DNS and LES for Simulating Stratocumulus: Better Together

J. P. Mellado[1] (iD) **, C. S. Bretherton[2]** (iD) **, B. Stevens[1]** (iD) **, and M. C. Wyant[2]** (iD)

[1] Max Planck Institute for Meteorology, Hamburg, Germany, [2] Department of Atmospheric Sciences, University of Washington, Seattle, WA, USA

Abstract We argue that combining direct numerical simulation (DNS) with large-eddy simulation (LES) and field studies could accelerate current lines of stratocumulus research. LES allows for a faster and more holistic study of the parameter space, but LES is sensitive to details of its formulation because the energetics are tied to unresolved processes in the cloud top region. One way to assess this sensitivity is through field studies. Another way is through DNS. In particular, DNS can be used to test the hypothesis that LES, even with an inadequate representation of the physics of cloud top entrainment, properly quantifies the sensitivity of cloud-topped boundary layers to changing environmental conditions. We support this argument by contrasting theoretical aspects of both techniques, by presenting first DNS results of a stratocumulus-topped boundary layer and discussing their convergence toward Reynolds number similarity, and by showing the consistency of DNS results with LES results and field measurements.

1. Introduction

Characterizing the dynamics of stratocumulus-topped boundary layers and their sensitivity to changing environmental conditions remains a challenge despite continuing efforts (Lilly, 1968; Wood, 2012). One reason is that such boundary layers compound very diverse phenomena that interact over a very broad range of scales. Whereas some interactions are well understood, even if quantifying their combined effect is sometimes difficult, some other interactions remain unclear, in particular, at meter and submeter scales in the entrainment zone. In this paper, we discuss the combination of large-eddy simulation (LES) and direct numerical simulation (DNS) to advance this characterization.

Since the pioneering works by Deardorff (1980) and Moeng (1986), LES has often been used for process studies of the stratocumulus-topped boundary layer. There is the consensus that LES is able to reproduce qualitatively many important properties, both when the cloud and subcloud layers are strongly coupled and the cloud cover is close to one (Kurowski et al., 2009; Stevens et al., 2005; Yamaguchi & Feingold, 2013; Yamaguchi & Randall, 2012), and when the cloud and subcloud layers start to decouple and the stratocumulus breaks into shallow cumulus (de Roode et al., 2016; McGibbon & Bretherton, 2017; Sandu & Stevens, 2011; van der Dussen et al., 2013). More recently, LES has also shown robustness in climate change sensitivity studies (Blossey et al., 2013; Bretherton & Blossey, 2014; Bretherton et al., 2013).

Quantitative prediction, however, remains difficult. There remains a large uncertainty in the dependence of cloud cover on the inversion jumps of thermodynamic properties (Lock, 2009; Mellado, 2017; Moeng, 2000; Sandu & Stevens, 2011; van der Dussen et al., 2014). Predicting the cloud cover during the stratocumulus-to-cumulus transition is also challenging. Although the main mechanism for transition is well understood, namely, the increase of surface latent heat flux caused by the increase of sea surface temperature, the cloud cover delicately depends on subsidence, long-wave radiative cooling, and precipitation (Sandu & Stevens, 2011; Yamaguchi et al., 2017). Another example where quantitative prediction remains difficult is climate change sensitivity studies, where the simulated sensitivity is comparable to the intramodel variability (Blossey et al., 2013; Bretherton et al., 2013). LES convergence studies with respect to the reduction of grid spacing would help to interpret these uncertainties, but these studies have not reached resolutions at which convergence is clearly occurring.

The difficulty of quantitative prediction is mainly attributed to an inadequate representation of cloud top entrainment. The strong radiative cooling atop stratocumulus clouds maintains a sharp inversion as little as 5-m thick, and turbulent entrainment through this stably stratified thin region is a critical feedback on the boundary layer and cloud properties. This entrainment is driven not only by large turbulent eddies but also
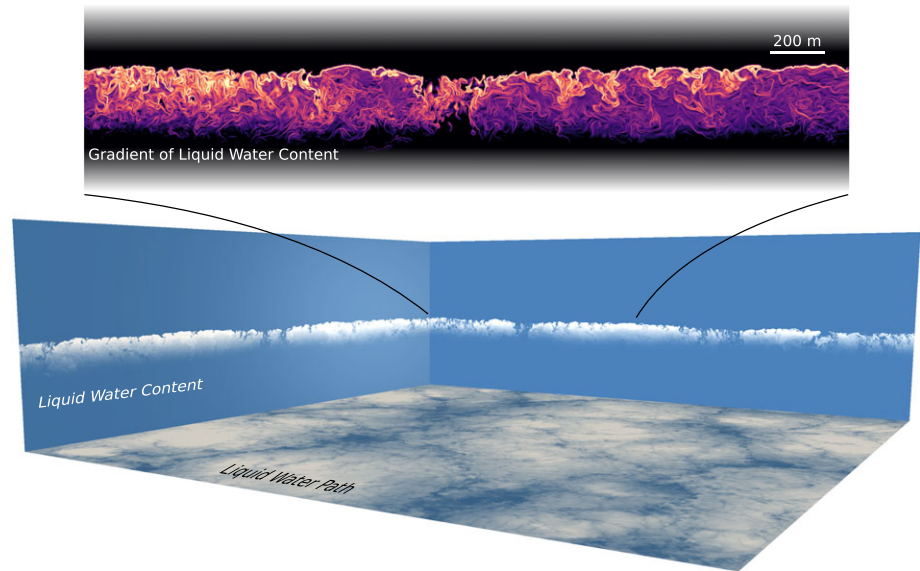
Figure 1. Composite of two vertical cross sections of liquid water content, a zoomed region on top with the gradient magnitude, and a bottom horizontal plane showing the liquid water path. Data corresponds to the direct numerical simulation case $\eta_0 = 0.7$ m at $t \approx 4.0$ hr (see Table 1).

by radiative and evaporative cooling in a narrow cloud top region, which allows cloud microphysics to also play an important role. Hence, the challenge is to simulate both the large turbulent eddies that dominate the interior of the boundary layer and the small-scale motions that drive entrainment (Figure 1).

Because LES accurately simulates the large turbulent eddies, LES successfully represents observed large-scale properties once the entrainment rates have been properly tuned. This success is often extended to what we call the *LES hypothesis*: *LES, even with an inadequate representation of cloud top entrainment, adequately quantifies the sensitivity of cloud-topped boundary layers to changing environmental conditions*. Having accurate reference data to properly tune the entrainment rate is a key element in this use of LES. Measurements suggest that LES can increasingly approximate a well-observed case when steps are taken to match the true entrainment rate given the observed vertical thermodynamic and cloud structure, for example, by choice of grid resolution and aspect ratio, advection scheme, or subgrid-scale turbulence model. However, the failure of LES to physically capture small-scale processes that are at least approximately responsible for entrainment at the top of stratocumulus clouds weakens our confidence in the LES results when entrainment rates tuned for some environmental conditions are used in another condition. One way to test this is through an expensive program of experimentation, and even this is not guaranteed to succeed. Another way is through DNS, which is what we propose in this paper. To this aim, we contrast theoretical aspects of DNS and LES and review recent studies in section 2, we present first DNS results of a stratocumulus-topped boundary layer in section 3, and we discuss the complementariness of DNS and LES in section 4.

2. Cloud Top Entrainment: A Challenge for DNS and LES

Simulating the full range of turbulence scales in Earth's atmospheric boundary layer is currently impractical. Consider a turbulent boundary layer in a fluid of kinematic viscosity ν whose most energetic eddies of aspect ratio $O(1)$ have a velocity scale U and a length scale comparable to the boundary layer depth H, and hence a characteristic turbulent dissipation rate $\varepsilon \sim U^3/H$. For a typical stratocumulus-topped boundary layer, one finds $H \sim 1$ km, $U \sim 1$ m/s, and $\varepsilon \sim 10^{-3}$ m²/s³. The Kolmogorov length scale $\eta \equiv (\nu^3/\varepsilon)^{1/4}$ characterizing the average size of the small, dissipative motions is only $\eta \sim 1$ mm, and the Reynolds number

$$\mathrm{Re}_0 \equiv HU/\nu \tag{1}$$

is comparatively large, $O(10^8)$. The range of length scales that must be covered is $H/\eta \sim \mathrm{Re}_0^{3/4} \sim 10^6$. A three-dimensional simulation with $O(10^6)$ points in each direction is far beyond current computational capabilities.

LES and DNS cope differently with this limitation. In LES, the Navier-Stokes equations are low-pass filtered and closed with a subgrid-scale model that represents the effect of the unresolved scales on the resolved ones (Fox & Lilly, 1972, 1967; Pope, 2000, 2004; Rogallo & Moin, 1984; Smagorinsky, 1963; Stevens & Lenschow, 2001). The underlying rationale is that large turbulent eddies account for most of the vertical transport and thus for most of the boundary layer dynamics, and they are most affected by the boundary conditions and hence less universal, whereas small turbulent eddies inside the inertial range of the turbulence cascade are more universal and isotropic and hence easier to model. In DNS, the original Navier-Stokes equations are retained and all atmospheric parameters except one, the Reynolds number, or, equivalently, the molecular viscosity, are matched (Moin & Mahesh, 1998; Orszag & Patterson, 1972; Pope, 2000). The underlying rationale is that the Navier-Stokes equations are an exceptionally good model for describing fluid motion under typical atmospheric conditions, and we understand relatively well all terms in those equations.

Effectively, both DNS and LES are currently restricted to low-to-moderate Reynolds numbers and their success partly relies on Reynolds number similarity. In DNS, the restriction to low-to-moderate Reynolds numbers appears directly in the governing equations through the kinematic viscosity ν. In LES, this restriction appears indirectly through the filter size Δ, an additional control parameter in the filtered equations. The dependence on Δ can be expressed as a dependence on a subgrid-scale viscosity that is much larger than the air molecular viscosity, which in turn can be expressed as an effective Reynolds number that is much smaller than the atmospheric value. Numerical dissipation tends to further reduce this effective Reynolds number (Sullivan & Patton, 2011). This restriction to low-to-moderate Reynolds numbers can be equivalently expressed as a restriction to low-to-moderate ranges of scales. The range of scales is H/η in DNS and H/Δ in LES, and the grid spacing needs to be commensurate with η in DNS and with Δ in LES. If the grid spacing is much larger than η, the DNS should diverge because the turbulent cascade continuously transfers energy toward the smallest resolved scales, where this energy would increasingly accumulate because the viscous dissipation at those scales is negligible. If the simulation does not diverge, then the numerical scheme is working de facto as a subgrid-scale turbulence model with a filter size commensurate with the grid spacing—this is the basis for implicit LES schemes (Domaradzki et al., 2003; Margolin & Rider, 2002; Smolarkiewicz & Margolin, 1998). The maximum range of scales in current simulations is $O(10^3)$, which means $Re_0 \sim 10^4$.

Reynolds number similarity is the experimental observation that relevant properties of turbulent flows become practically independent of the Reynolds number when this parameter surpasses some critical value Re_{crit} (Monin & Yaglom, 2007; Tennekes & Lumley, 1972). Although the exact value depends on the particular flow and property being considered, the order of magnitude of the critical Reynolds number is $10^3 - 10^4$, or, equivalently, a Taylor-based Reynolds number on the order of $100 - 150$ (Dimotakis, 2000). Beyond these values, statistical properties that exhibit Reynolds number similarity are equally well described by DNS and LES. Current computational resources start to reach those critical Reynolds numbers, which explains why DNS and LES results are becoming comparable with each other.

Problems appear when the grid spacing is not inside the inertial range of the turbulence cascade, and simulation results depend on the (effective) Reynolds number, on the subgrid-scale model, and on the numerical scheme, which casts doubt on the hypothesis that LES can correctly capture the sensitivity of large-scale properties to changes in the external control parameters despite not resolving the underlying processes. This occurs in the inversion atop stratocumulus clouds. Suppose the buoyancy jump across the inversion is Δb, which is 0.2 m/s^2 for a typical virtual-temperature jump of 7 K. Parcel arguments (Emanuel, 1994; Turner, 1973) imply that large-eddy updrafts can penetrate a distance commensurate with

$$\delta_{EZ} \equiv U^2/\Delta b \qquad (2)$$

above the mean inversion height. Thus, this penetration depth, which is 5 m for the typical parameters given above, scales the entrainment zone thickness. It is commonly assumed that it is necessary to resolve this thickness to simulate a reasonable entrainment rate that is not dominated by numerical diffusion. In turn, simulating a reasonable entrainment rate is necessary to appropriately represent the cloud top structure and thereby the cloud top turbulence forcing that characterizes stratocumulus-topped boundary layers. Indeed, LES studies with 5-m vertical resolution near the inversion have shown skill in simulating the liquid water path (LWP) of observed stratocumulus clouds, which is highly sensitive to entrainment, to within $25 - 50\%$ (Bretherton et al., 1999; Moeng, 2000; Stevens et al., 2005; Yamaguchi & Randall, 2008).

These studies also follow the common LES practice of using a large grid aspect ratio near a sharp inversion, with a horizontal grid spacing of $25 – 50$ m. An isotropic grid would be a natural choice where the inertial range of turbulence is resolved. However, LES of stratocumulus have traditionally produced overly efficient entrainment, manifest in simulated stratocumulus that are too thin or which break up prematurely compared with observations. Sensitivity studies suggest that for many LES models, the efficiency of entrainment for a given vertical grid spacing is reduced as the horizontal grid spacing is increased (e.g., Berner et al., 2011; Bretherton et al., 1999; Pedersen et al., 2016; Stevens et al., 1999). The choice of grid aspect ratio near the inversion can be regarded as a conscious or unconscious tuning that allows a simulation with inadequately resolved turbulence within the inversion to still maintain stratocumulus cloud layers of realistic thickness. For a given grid, the relation between entrainment efficiency and stratocumulus thickness also varies between LES models with different advection schemes and subgrid-scale turbulence models (e.g., Blossey et al., 2013; Pressel et al., 2017; Stevens et al., 1999, 2000, 2005), underlining that numerical convergence (in the sense of independence of simulated results from the choice of grid and numerical method) has not been achieved at these grid resolutions. Nevertheless, it is encouraging that one choice of LES grid can suffice to realistically simulate stratocumulus LWPs across a range of cloud regimes and inversion strengths (McGibbon & Bretherton, 2017) and that stratocumulus-to-cumulus transitions simulated by a variety of LES with the same grid resolutions all show similar and realistic evolutions (van der Dussen et al., 2013).

Figure 2 illustrates the dependence of stratocumulus thickness on the horizontal and vertical grid spacing for one LES using the DYCOMS-II RF01 nocturnal stratocumulus benchmark case (Stevens et al., 2005). The System for Atmospheric Modeling (Khairoutdinov & Randall, 2003) is run using the Blossey and Durran (2008) advection scheme and an anisotropic eddy viscosity for momentum and scalars. The original benchmark case is simplified slightly following Uchida et al. (2010) by removing both the radiative cooling and the increased stratification above the inversion. The LES was run with 5-, 10-, and 20-m vertical grid spacings, Δz, and 10-, 20-, 35-, 100-, and 250-m horizontal grid spacings, Δx. Each grid configuration is shown as an open circle in each figure panel. The colored contour lines contour the 3- to 6-hr hour mean value of the field plotted in each panel based on these LES grid configurations. The results are compared with the higher-resolution DNS of the same case to be discussed later, which are shown by triangles filled by the color corresponding to the simulated value (for the DNS grid, a 3.4- to 4.1-hr mean is used in place of the 3- to 6-hr mean). The short dashed line shows the 1:1 line corresponding to an isotropic grid.

All four panels show systematic variations of the simulated fields with LES grid resolution. The LWP shown in panel (a) and the low cloud fraction shown in panel (b) both increase as Δx increases for a fixed Δz, and both decrease as Δz increases for a fixed Δx or for a fixed aspect ratio $\Delta x / \Delta z$. For the LWP, the LES matches the observational estimate of 60 g/m^2 for $\Delta z = 5$ m and $\Delta x = 35$ m, a configuration commonly used for LES of stratocumulus with this model. Lines parallel to the heavy dashed line connect configurations with roughly similar LWP and cloud fraction. This heavy dashed line corresponds to the power law fit $\Delta z / 2.5 = (\Delta x / 2.5)^{0.2}$ where the grid spacings are given in meters. For this LES, one can thus simulate the observed LWP using a range of vertical grid spacings, but a coarser Δz requires a larger aspect ratio. This line intersects the 1:1 isotropic grid line at $\Delta x = \Delta z = 2.5$ m. That suggests that with an isotropic grid, this LES would require a resolution of 2.5 m or less to approach the observed cloud characteristics. Panel (c) shows the resolved-scale vertical velocity variance averaged between the surface and the inversion height, and panel (d) shows the entrainment rate (which also slowly modifies the inversion height). These do not follow the same behavior, that is, for the same LWP, a coarser-resolution simulation will tend to have less resolved-scale vertical velocity variance and somewhat less entrainment, with a slightly lower cloud top and slightly lower cloud base. That is, coarser vertical grid resolution than 5 m cannot simultaneously mimic all the behavior of a 5-m LES or finer simulation. The choice of grid for simulating stratocumulus with an LES involves trade-offs between inaccuracies in different simulated quantities, reflecting the tuning dictated by imperfectly converged simulations. LES of stratocumulus can provide valuable predictions and usefully expose the sensitivities of stratocumulus to cloud-controlling parameters, but these predictions should always be tempered by the inherent uncertainties in the entrainment process due to underresolution of the inversion zone.

We must go to a scale much finer than δ_{EZ} before reaching the inertial range of the turbulence cascade. This scale is the Ozmidov scale (Dougherty, 1961; Ozmidov, 1965)

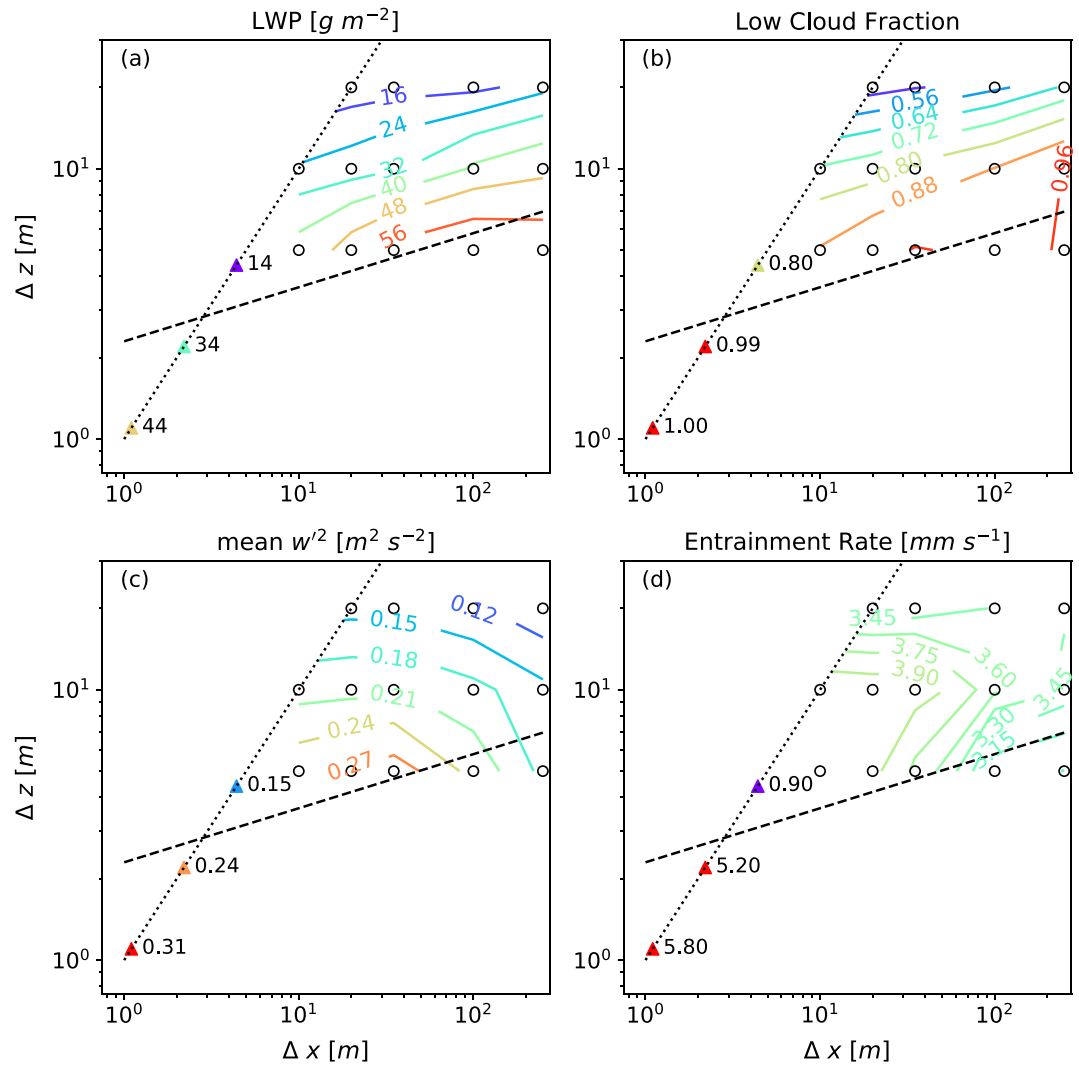$$\delta_{Oz} \equiv (\varepsilon / N^3)^{1/2} , \qquad (3)$$

Figure 2. Sensitivity to horizontal and vertical grid resolution of hour 3–6 mean statistics from large-eddy simulation (LES) of the DYCOMS-II RF01 nocturnal stratocumulus case: (a) liquid water path (LWP) (b) fraction of grid columns containing cloud, (c) boundary layer-mean-resolved vertical velocity variance, and (d) entrainment rate. Open circles indicate LES simulations, with colored contours interpolating between values from these simulations. Short dashed line is $\Delta z = \Delta x$. Long-dashed line is a fit to simulations consistent with the observed LWP, described in the text. Filled triangles are direct numerical simulation cases described later in the paper, colored as for the corresponding contours.

where N^2 is the mean buoyancy gradient. The Ozmidov scale is the crossover length scale at which the inertial breakup of the turbulence cascade and the restoring buoyancy force become equally important. According to the Richardson-Kolmogorov phenomenology, an eddy of size ℓ requires a turnover time $(\ell^2/\varepsilon)^{1/3}$ to break up into smaller motions. For $\ell \ll \delta_{Oz}$, this turnover time is much smaller than N^{-1} and the buoyancy force does not have time to restore equilibrium, the breakup proceeding unaffected. For $\ell \gg \delta_{Oz}$, the oscillatory motion induced by the restoring buoyancy force dominates the flow dynamics and mixing rates are reduced compared to a fully turbulent condition. If we assume $N^2 \sim \Delta b / \delta_{EZ}$, we find $N \sim \Delta b / U = 0.2$ s^{-1} and $\delta_{Oz} \sim 0.5$ m. This estimate is supported by observational studies (Katzwinkel et al., 2012; Jen-La Plante et al., 2016) and DNS studies (Mellado et al., 2014), which report an interval $\delta_{Oz} \sim 0.3$–4 m, depending on the environmental conditions. Hence, for fully explicitly resolved simulation of cloud top entrainment, we might need a grid spacing closer to 0.5 than to 5 m.

When reducing the grid spacing toward the Ozmidov scale and below, LES might converge faster than DNS because Newton's law of viscosity is an excellent model for molecular transport but not so for the inertial transfer through the turbulence cascade. In practice, however, combining DNS and LES might prove conve-

nient for several reasons. First, DNS reproduces bulk properties equally well and, in addition, DNS removes the variability introduced by subgrid-scale turbulence models and numerical artifacts, variability that complicates the comparison and interpretation of LES results obtained with different subgrid-scale models, different numerical schemes, or different grid properties — DNS data are fully characterized by one single parameter, a Reynolds number. Besides, the DNS-governing equations are better understood, so that DNS results can be more easily interpreted, in particular, for grid spacings near the Ozmidov scale where the interaction between turbulence and gravity waves is strong and still not fully understood (Ivey et al., 2008). Second, in DNS, the numerical uncertainty can be more clearly quantified through grid convergence studies, which facilitates to use analytical relationships derived from the original set of equations. For instance, we can derive entrainment rate equations that provide explicitly the mean entrainment velocity as the sum of contributions from different phenomena, like mixing, radiative cooling, evaporative cooling, and droplet sedimentation. This can be used for calculating and analyzing the mean entrainment velocity, and for assessing the various hypotheses behind existing parametrizations thereof. Last but not least, for a similar number of grid points, DNS becomes computationally cheaper than LES with explicit subgrid-scale models.

3. DNS of DYCOMS-II RF01

The challenge of resolving submeter scales, explained in the previous section, has motivated the use of DNS, but only in the cloud top region, partly sacrificing the representation of the effect of the large turbulent eddies that dominate the interior of the boundary layer (de Lozar & Mellado, 2015; Mellado, 2017; Mellado et al., 2010). The question is then, what is the skill of DNS in simulating the whole stratocumulus-topped boundary layer?

This section presents the first DNS of a stratocumulus-topped boundary layer. The aim is threefold. First, we show that DNS results agree with LES results in key properties describing the cloud and the turbulence structure. Second, we show that we are reaching the critical Reynolds numbers that mark the mixing transition toward Reynolds number similarity in those key properties. Third, we use DNS to discuss entrainment properties that are difficult to access using LES, such as the Ozmidov scale and the entrainment rate equation. All this provides the evidence to argue in section 4 that DNS can be used to test specific expressions of the LES hypothesis. We consider the first research flight of the DYCOMS-II field campaign because it has been extensively studied in the literature using measurements and LES, and because the persistence of a compact cloud under buoyancy reversal conditions challenges numerical simulations (Faloona et al., 2005; Kurowski et al., 2009; Matheou & Chung, 2014; Pedersen et al., 2016; Pressel et al., 2017; Stevens, Lenschow, Vali, et al., 2003; Stevens et al., 2005; Yamaguchi & Randall, 2008).

3.1. Description of the Simulations

We solve the Navier-Stokes equations in the anelastic approximation. We assume saturation adjustment, using the liquid water static energy, h, and the total-water specific humidity, q_t, as prognostic variables. We neglect droplet sedimentation. For the radiative flux, we use the one-dimensional model introduced by Stevens et al. (2005) and further discussed by Larson et al. (2007). A detailed description of the governing equations and the numerical algorithm is provided in Appendix A.

The control parameters corresponding to DYCOMS-II RF01 are set following Stevens et al. (2005). Initially, we set the boundary layer top at 840 m, and h and q_t vary between 294.7 kJ/kg and 9 g/kg below it and 303.3 kJ/kg and 1.5 g/kg above it. (The static energy retains the effect of composition on the specific heat, so that the enthalpy jump 8.5 kJ/kg corresponds to 10.5 kJ/kg when the dry-air heat capacity is used instead.) The surface pressure is 1017.8 hPa. The radiative transfer model is characterized by a net upward cloud top flux of 70 W/m^2, a net upward cloud base flux of 22 W/m^2, and a mass absorptivity factor of 85 m^2/kg. The sensible and latent heat fluxes at the surface are 15 and 117 W/m^2, respectively. The lapse rate in the free troposphere is zero: Two-dimensional sensitivity studies increasing the free troposphere static energy by 1.5 kJ/kg show negligible effects, and setting this lapse rate to zero allows us to neglect the free tropospheric radiative cooling. Subsidence is calculated with a constant divergence $D = 3.75 \times 10^{-6}$ s^{-1}.

The velocity components in the free troposphere are 7 and −5.5 m/s, and we model the surface layer as a solid no-slip boundary moving with constant velocity components 6 and −4.25 m/s, which are the mean values at the bottom of the mixed layer reported in Stevens et al. (2005, see also Figure C1 therein). This simplification removes the stringent resolution requirements necessary in the surface layer, where modeling the air-sea interaction is still a challenge (Richter & Veron, 2016; Sullivan & McWilliams, 2010). Although surface

Table 1
Study of Reynolds Number Dependence for DYCOMS-II RF01

Re_0	η_0	Grid spacing	$Re_{t,max}$	LWP	CF_{max}	$\eta_{z_{i,f}}$	$(\delta_{Oz})_{z_{i,f}}$
2000	2.8 m	4.4 m	280	13 g/m^2	0.68	4.1 m	6.4 m
5000	1.4 m	2.2 m	2720	34 g/m^2	0.96	1.8 m	4.8 m
12500	0.7 m	1.1 m	9410	44 g/m^2	0.99	0.9 m	3.2 m

Note. The last five columns are averages between $t = 3.4$ and $t = 4.1$ hr. Re_t is the turbulent Reynolds number, LWP is the liquid water path, CF is the cloud fraction, η is the Kolmogorov scale, δ_{Oz} is the Ozmidov scale, and $z_{i,f}$ indicates the height of minimum turbulent flux of liquid water static energy.

layer properties are modified by this simplification, in particular, the friction velocity in the DNS is ≈ 10 cm/s compared to the LES value ≈ 22 cm/s, we believe the conclusions of our work remain valid because turbulence is mainly driven by cloud top cooling, because the surface fluxes of moisture and static energy are fixed, and because we focus on the Reynolds number dependence of cloud layer and entrainment zone properties.

We consider three different Reynolds numbers Re_0 (see Table 1), where Re_0 is defined in equation (1). The reference length scale H is the initial boundary layer depth, that is, 840 m. The reference velocity scale is Deardorff's convective velocity scale $U \equiv (B_0 H)^{1/3}$ (Deardorff, 1970), where $B_0 \equiv g(\rho_0 c_0 T_0)^{-1} F_{r,ct}$ is the buoyancy flux associated with a cloud top radiative energy flux $F_{r,ct}$. For $F_{r,ct} = 70$ W/m^2, one finds $U = 1.18$ m/s. The control parameter Re_0 can be equivalently expressed in terms of a reference Kolmogorov scale $\eta_0 \equiv (\nu^3/B_0)^{1/4} = H\,Re_0^{-3/4}$. In this study, we vary η_0 by factors of two between $\eta_0 = 2.8$ and $\eta_0 = 0.7$ m.

The grid spacing is commensurate with the Kolmogorov scale, but it is more appropriate to identify each simulation with their value of η_0 or Re_0 instead of the grid spacing because different numerical schemes need different grid spacings for the same accuracy (Lele, 1992; Moin & Mahesh, 1998). For the compact, spectral-like schemes that we use, grid convergence studies have shown that a grid spacing less than $\approx 1.5\,\eta_0$ is sufficient for an accuracy better than $\approx 5\%$ in the budget of the turbulence kinetic energy (TKE) and the maximum gradients near the cloud top (Mellado, 2010) and near the surface (Mellado, 2012). The grid spacing in most of the computational domain is constant and equal in the three directions. Near the surface, refinement is needed to resolve the diffusive layer (Mellado, 2012), and, in the upper 20% of the domain, stretching is used to further separate the boundary of the computational domain from the turbulent flow. The grid sizes are $1,280^2 \times 384$, $2,560^2 \times 640$, and $5,120^2 \times 1,280$, and the computational domain is 5.6 km wide in both horizontal directions in all three cases.

Cases $\eta_0 = 2.8$ and $\eta_0 = 1.4$ m are initialized with random fluctuations in the liquid water static energy and in the total-water specific humidity. The power spectral density of these random fields peak at a wavelength equal to half of the boundary layer depth, and the profile of the resulting standard deviation smoothly increases from zero at the top and bottom of the boundary layer to a maximum 0.1 kJ/kg and 0.1 g/kg in the middle of the boundary layer. These two simulations are run for $\simeq 4.6$ hr. Case $\eta_0 = 0.7$ m uses the fields at $t = 2.6$ hr of case $\eta_0 = 1.4$ m as initial conditions, to reduce the spin-up time, and is run until $t = 4.1$ hr. Sensitivity studies with two-dimensional simulations indicate that, after approximately two large-eddy turnover times $2(z_i/w_{rms}) \approx 0.8$ hr from the beginning of case $\eta_0 = 0.7$ m, that is, after $t = 3.4$ hr, statistical properties from simulations initialized in this way become similar to the statistical properties from the simulations initialized with a random fluctuation at $t = 0$ hr (cf. Appendix B). The computational resources used for each simulation are 0.14, 2.5, and 20 million core hours, respectively, in the Blue Gene/Q system JUQUEEN at the Jülich Supercomputing Centre, using 8,192 cores for the two first simulations and 16,384 for the last one. The time step is calculated according to the Courant-Friedrichs-Lewy condition, and typical values toward the end of the simulations are 0.7, 0.2, and 0.06 s, respectively.

We compare statistical properties among the three simulations between $t = 3.4$ and $t = 4.1$ hr. Averaged over that period, the maximum turbulent Reynolds number $Re_t \equiv e^2/(\nu\varepsilon)$ is about 9400 (Table 1). In this definition, e is the turbulence kinetic energy, $\varepsilon \equiv \rho_{ref}^{-1}\langle \tau'_{ij}\partial_i u'_j \rangle$ is its viscous dissipation rate, and $\tau_{ij} = \mu(\partial_i u_j + \partial_j u_i)$ are the components of the viscous stress tensor. Henceforth, angle brackets indicate horizontal averages,
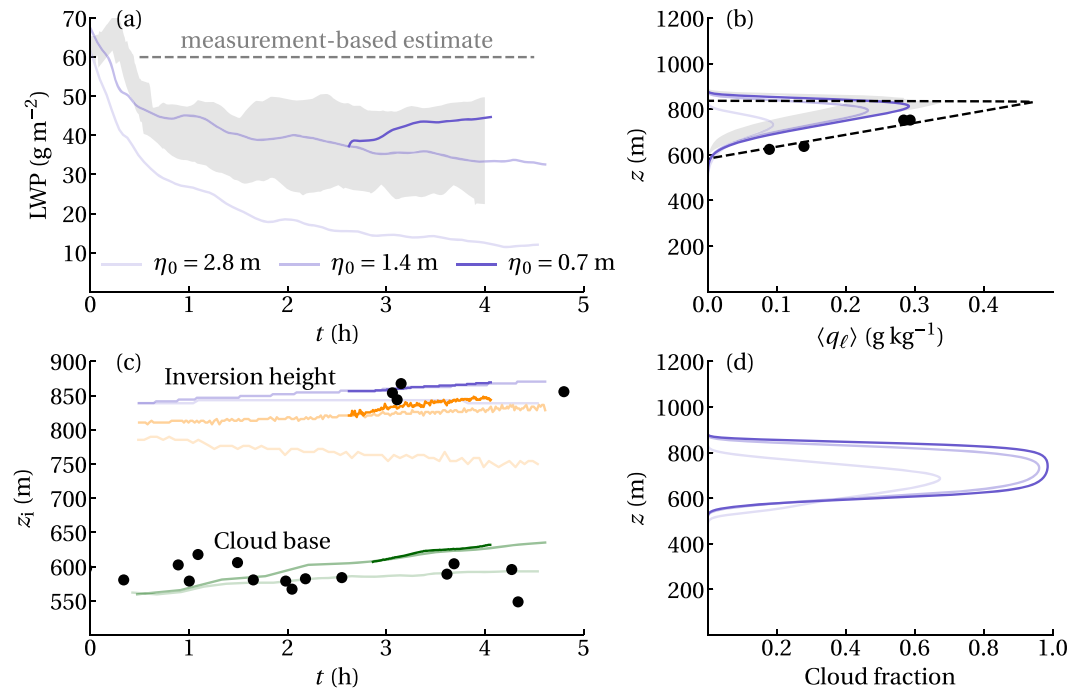
Figure 3. Liquid water properties, as represented by (a) the temporal evolution of liquid water path (LWP), (b) the vertical profiles of liquid water specific humidity, (c) the temporal evolution of inversion heights and cloud base heights, and (d) the vertical profiles of cloud fraction. The inversion heights are defined by the height of (blue) 50% relative humidity and (yellow) minimum turbulent flux of liquid water static energy. The cloud base height is defined by the lifting condensation level at 100 m. The cloud fraction is defined by the threshold 0.0047 g/kg (1% of the maximum adiabatic value). Vertical profiles are averaged between 3.4 and 4.1 hr. Gray region denotes the central half of the distribution of the large-eddy simulation ensemble in Stevens et al. (2005), as delimited by the first and third quartiles. Darker colors indicate higher Reynolds numbers as indicated in panel (a).

and apostrophes indicate the corresponding fluctuations. The corresponding Taylor-scale Reynolds number is $\sqrt{(20/3)Re_{t,max}} \approx 250$ (Pope, 2000), which is comparable to the values for mixing transition towards Reynolds number similarity observed in various turbulent flows (Dimotakis, 2000).

3.2. Results

Figure 3a shows that the temporal evolution of LWP in DNS qualitatively agrees with that observed in previous LES studies: there is a spin-up phase during the first simulation hour and a slow decrease thereafter toward a value smaller than measurement-based estimates. The DNS case with the largest Kolmogorov scale, $\eta_0 = 2.8$ m, is in the lowest quartile of the LES model ensemble considered by Stevens et al. (2005). However, the DNS case with $\eta_0 = 1.4$ m already reproduces the LES ensemble mean, which is about 35 g/m². Reducing the Kolmogorov scale further by a factor of 2 increases the LWP moderately, to ≈ 45 g/m². This Reynolds number dependence illustrates the convergence toward Reynolds number similarity when the Reynolds number approaches $Re_0 \sim 10^4$: the relative change in LWP between cases $\eta_0 = 2.8$ and $\eta_0 = 1.4$ m is $\approx 140\%$, whereas the relative change in LWP when reducing η_0 the same amount between cases $\eta_0 = 1.4$ and $\eta_0 = 0.7$ m is $\approx 30\%$. Reynolds number similarity is approached faster in the inversion height, cloud base height, and cloud fraction (Figures 3b–3d). In particular, peak cloud fractions close to one are already obtained for $\eta_0 = 1.4$ m (see also Table 1). The compact character of the cloud is further illustrated in Figure 1.

The turbulence structure, as represented by the variance and third-order moment of the vertical velocity, shows a Reynolds number dependence that is similar to that found in the liquid water properties discussed before. As seen in Figure 4, the DNS with the lowest Reynolds number represents the lower quartile of the LES ensemble in Stevens et al. (2005). For this case, the variance in the center of the boundary layer is ≈ 3 times smaller than the measurements. The variance also exhibits a local minimum near the cloud base, a minimum that is often associated with decoupling between the cloud and the subcloud layers. This behavior is consistent with the low LWP observed before and the resulting reduction of the cloud top radiative forcing, which is the main source of turbulence in this type of boundary layer. Concomitantly, the third-order moment
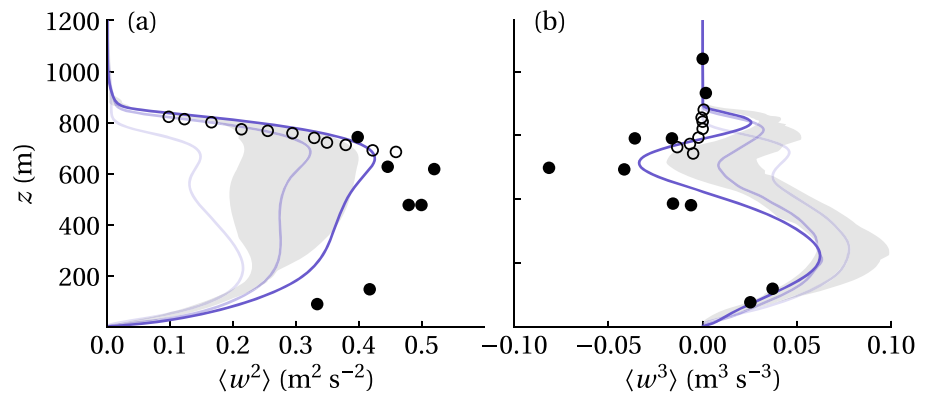
Figure 4. Turbulence structure, as represented by the vertical profiles of (a) the second-order moment and (b) the third-order moment of the vertical velocity. Gray region denotes the central half of the distribution of the large-eddy simulation ensemble, and circle markers indicate estimates derived from in situ (filled circles) and radar (open circles) measurements, as reported in Stevens et al. (2005). Darker colors indicate higher Reynolds numbers as indicated in Figure 3a.

is positive throughout the boundary layer, which is interpreted as the predominance of strong updrafts induced by surface fluxes. When the Kolmogorov scale is reduced to $\eta_0 = 1.4$ m, DNS reproduces the LES ensemble mean. As the strength of the radiative forcing is better represented—the radiative flux divergence across the boundary layer approximately doubles, from ≈ 20 to ≈ 40 W/m^2 (not shown)—the variance increases, and the local minimum near the cloud base disappears. Concomitantly, the local minimum in the third-order moment near the cloud base approaches zero, indicating the increasing presence of strong downdrafts. For the largest Reynolds number, when $\eta_0 = 0.7$ m, the radiative flux divergence is ≈ 45 W/m^2, the variance in the DNS already reproduces 75% of the measurements at most heights, and the third-order moment becomes negative near the cloud base and closely reproduces the measurements.

As explained in section 3.1, we have simplified the case by removing droplet sedimentation, finite rate phase change, and shear production of TKE near the surface. These phenomena affect the properties discussed above, and thus, a one-to-one agreement with measurements is not expected. It is remarkable, however, that DNS can reproduce the profiles not only qualitatively but also quantitatively to such a large extent, despite the Reynolds numbers in the simulations being much smaller than the atmospheric counterpart. Moreover, two-dimensional simulations of cases with $\eta_0 = 0.35$ and $\eta_0 = 0.18$ m yield a LWP that is similar to the LWP of case $\eta_0 = 0.70$ m (cf. Appendix B). Although two-dimensional problems have some different physics than three-dimensional problems, this result further indicates that the dependence on Reynolds number that we start to reach in some important properties is comparable or smaller than the uncertainty associated with statistical convergence in simulations and measurements.

To better understand the observed convergence of DNS toward measurements and Reynolds number similarity, we investigate the energetics of the flow, in particular the liquid water static energy and the kinetic energy in the cloud layer and in the entrainment zone. The static energy flux is plotted in Figure 5a, where we see a qualitative change between the cases $\eta_0 = 2.8$ and $\eta_0 = 1.4$ m. For $\eta_0 = 2.8$ m, the flux is negative in the whole cloud layer and the maximum molecular contribution near the cloud top is twice the maximum turbulent contribution. When the Kolmogorov scale is reduced to $\eta_0 = 1.4$ m, the flux is negative only at the cloud top and the maximum turbulent and molecular contributions become comparable. When we further reduce the Kolmogorov scale to $\eta_0 = 0.7$ m, the flux in the cloud layer further increases as the cloud top cooling is better resolved and the downdrafts become colder and stronger. Better resolving the inversion mixing processes is important to properly capture the relative importance of radiative and evaporative cooling, since reducing the erosion of the simulated cloud top leads to an optically thicker cloud with greater radiative cooling, and also leads to less mixing and a weaker evaporative cooling (de Lozar & Mellado, 2015). In the entrainment zone, the molecular contribution decreases significantly and becomes approximately half of the turbulent contribution for $\eta_0 = 0.7$ m, so that turbulence starts to dominate. Besides, the turbulent contribution in the entrainment zone remains similar between the two largest Reynolds numbers, which indicates the emergence of Reynolds number similarity in the entrainment drying and warming of the cloud.
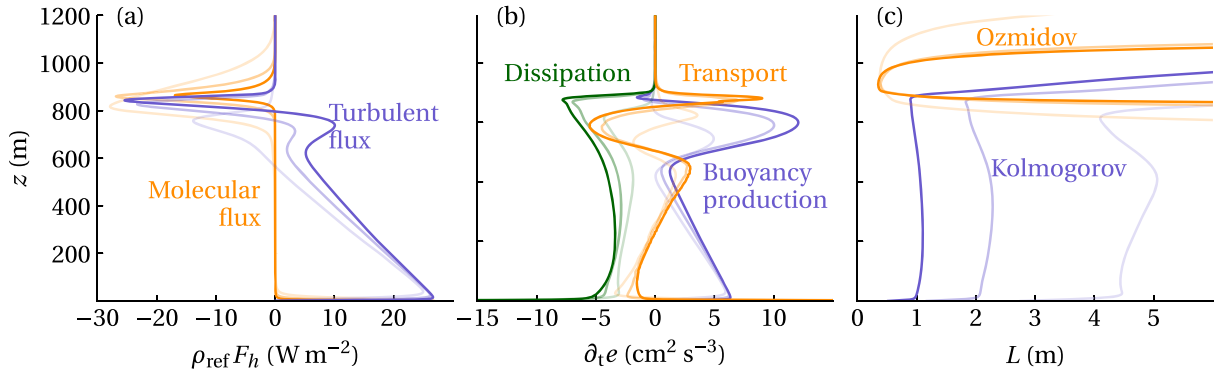
Figure 5. Energetics, as represented by the vertical profiles of (a) the flux of liquid water static energy, (b) the budget of turbulence kinetic energy, and (c) the Kolmogorov scale, $\eta \equiv (\nu^3/\varepsilon)^{1/4}$, and the Ozmidov scale, $\delta_{\mathrm{Oz}} \equiv (\varepsilon/N^3)^{1/2}$. Darker colors indicate higher Reynolds numbers as indicated in Figure 3a.

The behavior of the TKE budget with the Reynolds number is consistent with that of the vertical velocity component and of the flux of liquid water static energy. For the lowest Reynolds number, the buoyancy flux near the cloud base is approximately zero, which indicates a tendency toward decoupling (Figure 5b). However, when we increase the Reynolds number from $Re_0 = 2000$ to $Re_0 = 5000$, the buoyancy flux profile becomes top heavy and the local minimum near the cloud base becomes increasingly positive. Since the buoyancy flux is the main TKE source, the magnitudes of the viscous dissipation rate and the turbulent transport rate increase commensurately with the increase of buoyancy flux. When we further increase the Reynolds number from 5000 to 12500, the change in the TKE budget is much smaller, indicating again the tendency towards Reynolds number similarity.

The observed behavior in liquid water properties, turbulence structure, and energetics indicates a qualitative change at about 1-m grid spacing in the skill of DNS to represent turbulence in the cloud layer and in the entrainment zone. Section 2 has explained the importance of the Ozmidov scale in the cloud top region, which motivates us to study this quantity, in particular, in comparison with the Kolmogorov scale. Research in stratified turbulence has shown that the Ozmidov scale must be larger than the Kolmogorov scale for turbulence to be maintained, since motions larger than the Ozmidov scale are dominated by the restoring buoyancy force instead of the inertial transfer characterizing the turbulence cascade (see, e.g., Chung & Matheou, 2012; Herbert & de Bruyn Kops, 2006). This comparison is presented in Figure 5c, where we see that the Ozmidov scale is larger than the Kolmogorov scale in most of the boundary layer except near the cloud top, where both scales become comparable. This is more clearly quantified in Table 1 by comparing the values at the height of minimum turbulent flux of liquid water static energy, $z_{\mathrm{i,f}}$. With increasing Reynolds number, the Kolmogorov and Ozmidov scales at that height decrease, the former following the control parameter η_0 and the latter following the buoyancy gradient increase. The ratio $(\delta_{\mathrm{Oz}}/\eta)_{z_{\mathrm{i,f}}}$, however, is larger than one and increases with increasing Reynolds number, which provides another indication of turbulence increasingly dominating the cloud top dynamics. In particular, this ratio is $(\delta_{\mathrm{Oz}}/\eta)_{z_{\mathrm{i,f}}} \approx 4$ for $\eta_0 = 0.7$ m, which, although moderate, seems sufficient for the simulations to reproduce observed cloud and boundary layer properties to a large extent.

The observed convergence toward Reynolds number similarity around 1-m grid spacing is further confirmed by the analysis of the mean entrainment velocity. Following Lilly (1968), we define the mean entrainment velocity as

$$w_{\mathrm{e}} \equiv \frac{\mathrm{d}z_{\mathrm{i}}}{\mathrm{d}t} - \langle w \rangle_{z_{\mathrm{i}}} , \tag{4}$$

where $z_{\mathrm{i}}(t)$ is an arbitrary height identifying the boundary layer top, a function of time only, and $\langle w \rangle_{z_{\mathrm{i}}}$ is the mean vertical velocity at that height. The subscript z_{i} next to a variable indicates that the variable is evaluated at $z = z_{\mathrm{i}}$. The integral analysis of the evolution equations in a control volume extending from z_{i} upward to a height z_{∞} in the free troposphere yields the following class of expressions (cf. Appendix A)

$$w_{\mathrm{e}}(\langle \phi \rangle - \phi_{\mathrm{bg}})_{z_{\mathrm{i}}} = F_{\phi,z_{\mathrm{i}}} - F_{\phi,\infty} + \int_{z_{\mathrm{i}}}^{z_{\infty}} (S_{\phi} + \rho_{\mathrm{ref}}\, \gamma_{\phi} \langle w \rangle)\, \mathrm{d}z + \frac{\mathrm{d}}{\mathrm{d}t} \int_{z_{\mathrm{i}}}^{z_{\infty}} (\phi_{\mathrm{bg}} - \langle \phi \rangle)\, \mathrm{d}z , \tag{5}$$
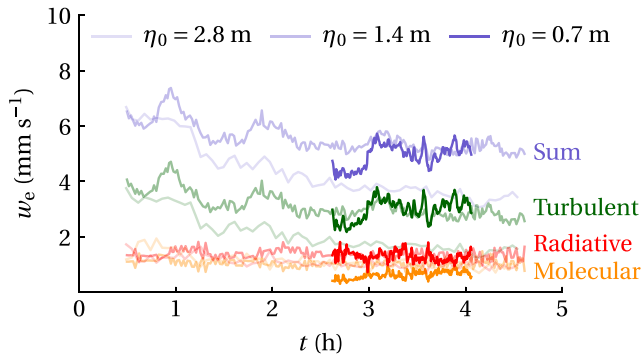
Figure 6. Temporal evolution of the various contributions to the mean entrainment velocity according to equation (6) evaluated at the height of minimum turbulent flux of liquid water static energy. Darker colors indicate higher Reynolds numbers as indicated for the sum.

where ϕ indicates an arbitrary property per unit volume, F_ϕ is the average flux of ϕ, S_ϕ is a source term, $\phi_{bg}(z)$ is the background profile describing the unperturbed atmosphere without the turbulent boundary layer, and $\gamma_\phi \equiv -d_z(\phi_{bg}/\rho_{ref})$ is the corresponding lapse rate. The accumulation term at the end quantifies unsteady effects that manifest as a deformation of the cloud top mean structure in a frame of reference moving with z_i. We refer to this class of expressions as entrainment rate equations. These equations allow us to quantify the contributions from various phenomena to w_e (Mellado, 2017), and they recover the jump relations used in mixed-layer models when the mixed-layer model approximations to the actual solutions are substituted into them (Stevens, 2002).

We have studied this equation for the liquid water static energy per unit volume, that is, $\phi = \rho_{ref} h$, with the inversion height specified as the height of minimum turbulent flux, $z_{i,f}$. For this variable, the source term is zero, the lapse rate of the background profile is zero, and the flux contains a turbulent contribution, a molecular contribution, and a radiative contribution, so that we can rewrite equation (5) as

$$w_e = w_e^{tur} + w_e^{mol} + w_e^{rad} + w_e^{def} . \tag{6}$$

As observed in Figure 6 and Table 2, the simulated mean entrainment velocity is between 5 and 6 mm/s for $\eta_0 = 1.4$ m or smaller, which agrees with measurements (Faloona et al., 2005; Stevens, Lenschow, Faloona, et al., 2003). We also observe that the change of w_e between cases $\eta_0 = 2.8$ and $\eta_0 = 1.4$ m is about 60%, but the change between $\eta_0 = 1.4$ and $\eta_0 = 0.7$ m is about 15%, supporting again the tendency towards Reynolds number similarity observed in the previous statistical properties. This is further confirmed by the analysis of the various contributions to w_e. We observe that the turbulent contribution increases substantially when decreasing η_0 between 2.8 and 1.4 m, becoming the dominant term in equation (5), and it changes much less when reducing η_0 another factor of 2. For the Reynolds numbers achieved in our simulations, the molecular contribution is still comparable to the radiative contribution, which might explain the difficulty to quantify the direct effect of radiation on entrainment in numerical simulations with a grid spacing of several meters. However, the radiative contribution is only 20% of w_e, making this uncertainty less relevant for the particular stratocumulus condition studied here.

Table 2 also shows a strong effect of the deformation term for case $\eta_0 = 2.8$ m, indicating the lack of quasi-steadiness in the entrainment zone for that condition, which further complicates the analysis of entrainment. Because the deformation term varies in time, we calculate it by fitting an exponential function to the integral term in equation (5) and evaluating its time derivative at $t = 4.1$ hr (Figure 7). The deformation term in case $\eta_0 = 0.7$ m is still nonnegligible after 1.5 hr from the initial condition, and it accounts for most of the difference in w_e between cases $\eta_0 = 1.4$ and $\eta_0 = 0.7$ m, but it is decreasing towards zero as the subsidence sharpens the relatively thick initial inversion from case $\eta_0 = 1.4$ m. Hence, the mean entrainment velocity obtained in DNS is likely closer to 5 than to 6 mm/s, which agrees with the upper limit of measurement-based estimates (Faloona et al., 2005; Stevens, Lenschow, Faloona, et al., 2003).

In summary, current computational resources allow us to reach Reynolds numbers that are sufficiently large for DNS to reproduce field measurements. Physically, this skill relies on the capability to partly simulate flow motions that are commensurate with the Ozmidov scale in the entrainment zone, so that wave-like motions, which do not mix scalars very efficiently, are partly resolved. The implication is that LES can be used to form specific hypotheses about important stratocumulus cloud-controlling factors that can be more rigorously tested with DNS rather than relying on field studies with all their uncertainties.

4. Prospectus

We argue that DNS and LES are complementary tools to understand nature, and combining them could accelerate current lines of stratocumulus research. LES allows for a faster and more holistic study of

Table 2
Reynolds Number Dependence of the Mean Entrainment Velocity

Re_0	η_0	w_e^{tur}	w_e^{mol}	w_e^{rad}	w_e^{def}	w_e
2000	2.8 m	1.6	1.0	1.0	−1.9	1.7
5000	1.4 m	2.8	1.0	1.4	−0.1	5.1
12500	0.7 m	3.1	0.7	1.2	0.9	5.9

Note. All velocities are in mm/s. Columns 3–5 are averages between $t = 3.4$ and $t = 4.1$ hr.
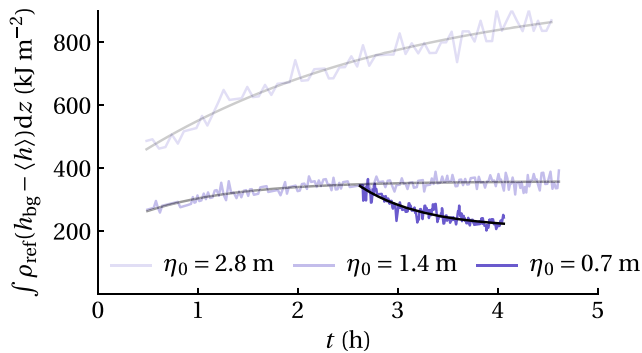
Figure 7. Temporal evolution of the integral term $\int_{z_i}^{z_\infty}(\phi_{bg} - \langle\phi\rangle)\,\mathrm{d}z$ in equation (5) evaluated for $\phi = \rho_{ref}\,h$ at $z_i = z_{i,f}$, the height of minimum turbulent flux of liquid water static energy. Black lines indicate the least squares fits to $\beta_1 \exp(\beta_2 t) + \beta_3$.

stratocumulus-topped boundary layers and their role in a warming climate. This study has identified key processes that might be inadequately represented, such as the interaction between turbulence, evaporation, radiation, and microphysics at meter and submeter scales in the entrainment zone. DNS is particularly well suited to investigate these small-scale problems, which opens a new avenue to test specific expressions of the LES hypothesis that, even with an inadequate representation of the physics of cloud top entrainment, LES properly quantifies the sensitivity of cloud-topped boundary layers to changing environmental conditions.

This paper does not yet test this LES hypothesis but demonstrates that DNS is entering a regime that makes such tests possible. We have shown that ≈1-m resolution is sufficient to reproduce measurements from the first research flight of the DYCOMS-II field campaign with an accuracy of 5–25% depending on the property. That grid spacing is commensurate with the Ozmidov scale in the entrainment zone, so that we start to resolve the inertial range of the turbulence cascade, which helps explain the convergence towards Reynolds number similarity: As entrainment drying and warming becomes properly captured, the cloud top structure is better represented, the cloud top turbulence forcing is more accurate, and there is a better agreement between simulated and measured boundary layer and cloud properties. When changing the case, we need to investigate the dependence of the results on the Reynolds number, which can be computationally demanding. In exchange, however, DNS can be used as reference for grid convergence and intercomparison studies of LES models.

To test the LES hypothesis, we can investigate whether DNS exhibits similar sensitivities of the mean entrainment velocity to changing environmental conditions. We could quantify the extent to which entrainment can be thought of as a purely interfacial process and how much is driven from the large turbulent eddies, which would aid parametrization development for general circulation models. One possible experiment would be to consider a sudden change of surface fluxes, as caused, for instance, by a sudden change in wind speed. When does the mean entrainment velocity change? If local processes at or near the interface are controlling entrainment, this change should have little effect in time scales smaller than those necessary to change the mean properties of the boundary layer, namely, several large-eddy turnover times (Jones et al., 2014; van Driel & Jonker, 2010). If, on the other hand, entrainment is mainly controlled by the kinetic energy of large turbulent eddies, entrainment should increase quicker in response to the increased buoyancy flux. The question can be posed the other way around: For a given convective forcing, what is the sensitivity of the mean entrainment velocity to changes in evaporative cooling, droplet sedimentation, and shear broadening? Meter and submeter scales are believed to be important for these questions, and DNS opens a new window to look into these questions.

Last, DNS and LES can also be combined to study the evolution of the droplet size distribution, which is needed to characterize microphysics and aerosol effects. The study of the droplet size distribution arguably needs to substitute the Eulerian description of the liquid water with a Lagrangian description (Grabowski & Wang, 2013; Shaw, 2003; Stevens et al., 1996). Lagrangian studies of the droplet size distribution have often considered homogeneous isotropic turbulence, and we need to learn how the strong inhomogeneity, the stable stratification, and the various interfacial layers in the entrainment zone affect the characteristics and the evolution of the droplet size distribution. Besides, turbulence properties of the dissipative scales are known to depend on the Reynolds number (Lanotte et al., 2009; Onishi & Seifert, 2016). DNS can help understanding these effects of inhomogeneity and Reynolds number in the cloud top region, as it is helping in other cloud interfaces (Götzfried et al., 2017; Kumar et al., 2014; Perrin & Jonker, 2015), which could aid the development of super-droplet parametrizations, for example, to model the subgrid-scale velocity fluctuation or the subgrid-scale supersaturation (Chandrakar et al., 2016; Shima et al., 2009). At the same time, however, history effects might also be important and those depend on the large-scale variation of thermodynamic fields (de Lozar & Muessle, 2016; Grabowski & Abade, 2017; Naumann & Seifert, 2016), which would be more appropriately studied by means of LES. In summary, characterizing the evolution of the droplet size distribution in stratocumulus clouds is a challenge where both DNS and LES are needed.

5. Conclusions

We have contrasted theoretical aspects of DNS and LES, reviewed recent studies, and presented first DNS results of a stratocumulus-topped boundary layer to argue that combining DNS with LES and field studies could accelerate current lines of stratocumulus research. LES allows for a faster and more holistic study of the parameter space, identifying key processes that might be inadequately represented, such as cloud top entrainment. DNS is particularly well suited to investigate those processes, for instance, in the case of cloud top entrainment, the interaction between turbulence, evaporation, radiation, and microphysics at meter and submeter scales. Hence, LES can be used to form specific hypotheses, and DNS can be used to test those hypotheses without having to rely exclusively on field studies.

Like LES, DNS is restricted to low-to-moderate Reynolds numbers and its effects on the results need to be ascertained, which can be computationally demanding. In exchange, however, we obtain data that is freer of modeling and numerical uncertainty and that depends only on one single parameter, the Reynolds number, which facilitates comparison and interpretation of results. We have shown that current computational resources start to reach the critical Reynolds number necessary for Reynolds number similarity in key boundary layer and cloud properties. We have also shown that the ratio between the Ozmidov scale and the Kolmogorov scale in the entrainment zone is a good indicator, which can be understood because down-gradient turbulence models poorly represent wave-like motions, which do not mix scalars very efficiently.

One particular application of DNS is testing the LES hypothesis that, even with an inadequate representation of the physics of cloud top entrainment, LES properly quantifies the sensitivity of cloud-topped boundary layers to changing environmental conditions. For instance, DNS can be used as reference in LES convergence and intercomparison studies to better assess the accuracy of LES in capturing the sensitivity and response times of the mean entrainment velocity to changes of surface fluxes and inversion jumps of thermodynamic properties and velocity. This could help to reduce the intramodel variability of cloud properties in LES studies of stratocumulus-to-cumulus transition and climate change sensitivity. Another problem where combining DNS and LES seems valuable is the study of the droplet size distribution in the cloud top region, to ascertain the relative importance of statistical inhomogeneity and intermittency, stable stratification, and history effects.

Last but not least, the work presented here also demonstrates that we have a complete hierarchy of models that covers from planetary scales to sub-Kolmogorov scales, since we can compare one-to-one LES results from numerical models commonly used in climate research to DNS results from numerical models commonly used in turbulence research. This can facilitate a more seamless study of the multiscale character of the climate system.

Appendix A: Problem Formulation

The evolution equations are based on the anelastic approximation to the Navier-Stokes equations:

$$\nabla \cdot (\rho_{\text{ref}} \, \mathbf{u}) = 0 \, , \tag{A1}$$

$$\rho_{\text{ref}} \, D_t \mathbf{u} = -\nabla p + \mu \nabla^2 \mathbf{u} + g(\rho_{\text{ref}} - \rho) \, \mathbf{k} + \rho_{\text{ref}} \, \omega \, \partial_z \mathbf{u} \, , \tag{A2}$$

$$\rho_{\text{ref}} \, D_t h = \nabla \cdot [\rho \kappa_h \nabla h - \rho \mathbf{j}_\mu (h_\ell - h) - \rho \mathbf{j}_r] + \rho_{\text{ref}} \, \omega \, \partial_z h \, , \tag{A3}$$

$$\rho_{\text{ref}} \, D_t q_{\text{t}} = \nabla \cdot [\rho \kappa_v \nabla q_{\text{t}} - \rho \mathbf{j}_\mu (1 - q_{\text{t}})] + \rho_{\text{ref}} \, \omega \, \partial_z q_{\text{t}} \, , \tag{A4}$$

$$\rho_{\text{ref}} \, D_t q_\ell = \nabla \cdot [\rho \kappa_v \nabla q_\ell - \rho \mathbf{j}_\mu (1 - q_\ell)] + \rho(\partial_t q_\ell)_{\text{con}} + \rho_{\text{ref}} \, \omega \, \partial_z q_\ell \, , \tag{A5}$$

where D_t is the substantial derivative operator, ρ_{ref} is the reference density profile resulting from the reference hydrostatic balance, $\mathbf{u}$ is the velocity vector, g is the magnitude of the gravitational acceleration, $\mathbf{k}$ is the unitary vector pointing upward, ω is the large-scale subsidence velocity, q_{t} is the total-water specific humidity, q_ℓ is the liquid water specific humidity, h is the liquid water static energy, defined as

$$h \equiv [c_{\text{d}} + q_{\text{t}}(c_{\text{v}} - c_{\text{d}})]T - q_\ell L_{\text{v}} + gz \, , \tag{A6}$$

and $h_\ell \equiv h|_{q_\ell=1}$ is the static energy of liquid water. The enthalpy of vaporization varies with the temperature as $L_v = L_v^0 - (c_\ell - c_v)(T - T^0)$, using 2.4429 MJ/kg at $T^0 = 298.15$ K. The specific heat capacities at constant pressure of dry air, c_d, water vapor, c_v, and liquid water, c_ℓ, are constant.

A detailed discussion of the assumptions and their accuracy leading to these equations can be found in Mellado et al. (2010) and de Lozar and Mellado (2014), and we only summarize the main aspects here. These evolution equations assume that the thermal diffusivity κ_h is equal to the diffusivity of water vapor in dry air κ_v; for typical atmospheric conditions, one finds $\kappa_h/\kappa_v \approx 0.8$. They further neglect the dependence of the air dynamic viscosity μ on T, which is small for the range of temperatures that we are interested in. The liquid mass flux

$$\rho \mathbf{j}_\mu \equiv -\rho q_\ell \left[\overline{d^5} / \left(\overline{d^3} d_0^2 \right) \right] w_s \mathbf{k} - (\rho\kappa_\ell - \rho\kappa_v)(1 - q_\ell)^{-1} \nabla q_\ell \tag{A7}$$

accounts for the fluxes due to gravitational settling and differential diffusion. In this definition, $\overline{d^n}$ is the nth moment of the droplet size distribution, $w_s \equiv g\rho_\ell d_0^2/(18\mu)$ is the settling velocity of a droplet with a diameter d_0 and density ρ_ℓ, and κ_ℓ is the diffusivity of the liquid phase into the gaseous phase. The condensation rate is given by

$$\rho(\partial_t q_\ell)_{con} \equiv \rho q_\ell \left[\bar{d} d_0^2/(\overline{d^3}) \right] \frac{q_v/q_s - 1}{t_{p,0}} , \tag{A8}$$

where the numerator is the supersaturation and the denominator is the phase relaxation time of a droplet with diameter d_0, $t_{p,0} \equiv d_0^2/(12\gamma)$, where $\gamma \approx 10^{-10}$ m²/s (Rogers & Yau, 1989).

For the work presented in this paper, we assume saturation adjustment and drop equation (A5). The saturation vapor pressure is calculated with the polynomial fit provided by Flatau et al. (1992). We also neglect the liquid mass flux $\rho \mathbf{j}_\mu$. Further, we assume $\mu/(\rho\kappa_h) = 1$, that is, a Prandtl number equal to 1, which is a good approximation for typical atmospheric values, ≈ 0.7. The radiative flux is modeled as (Larson et al., 2007; Stevens et al., 2005)

$$\rho \mathbf{j}_r \equiv \left\{ F_{r,ct} e^{-\kappa LWP_z} - F_{r,cb} e^{-\kappa(LWP_0 - LWP_z)} \right\} \mathbf{k} , \tag{A9}$$

where κ is the mass absorptivity factor and

$$LWP_z \equiv \int_z^{z_\infty} \rho_{ref} q_\ell d\zeta . \tag{A10}$$

The evolution equations are solved using finite-difference approximations based on spectral-like sixth-order compact Padé schemes (Lele, 1992). Biased formulas are employed at the top and bottom boundaries (Carpenter et al., 1993). Time advancement is performed with low-storage Runge-Kutta schemes (Carpenter & Kennedy, 1994). The algorithm to solve the pressure-Poisson equation is based on a Fourier decomposition in the horizontal planes, which leads to a set of difference equations along the vertical direction. A factorization thereof is used to satisfy equation (A1) to machine accuracy (Mellado & Ansorge, 2012). Source files with the implementation of this numerical algorithm and further documentation can be found at https://github.com/turbulencia/tlab.

The entrainment rate equation used in section 3.2 can be derived from the integral analysis of the evolution equation

$$\partial_t \langle \phi \rangle = -\partial_z F_\phi + S_\phi + \partial_z(\omega\langle\phi\rangle) , \tag{A11}$$

where $\langle\phi\rangle$ denotes the mean of an arbitrary variable per unit volume ϕ, F_ϕ is the corresponding mean vertical flux, and S_ϕ is the source term. For instance, applied to the liquid water static energy, we find $\langle\phi\rangle = \rho_{ref}\langle h\rangle$,

$$F_h = \rho_{ref}\langle w'h'\rangle - \rho\kappa_h\partial_z\langle h\rangle + \langle\rho\mathbf{j}_\mu(h_\ell - h)\rangle\cdot\mathbf{k} + \langle\rho\mathbf{j}_r\rangle\cdot\mathbf{k} , \tag{A12}$$

and $S_h = 0$. We have assumed statistical homogeneity in the horizontal directions. Integrating equation (A11) from an arbitrary height $z_i(t)$ upward to a height z_∞ in the free troposphere yields

$$\int_{z_i}^{z_\infty} \partial_t \langle\phi\rangle \, dz = F_{\phi,z_i} - F_{\phi,\infty} + \int_{z_i}^{z_\infty} S_\phi \, dz + \int_{z_i}^{z_\infty} \partial_z(\omega\langle\phi\rangle) \, dz . \tag{A13}$$
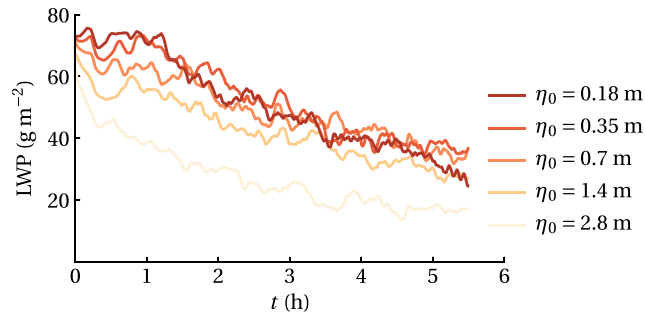
Figure B1. Sensitivity of liquid water path (LWP) to changes in Reynolds number in two-dimensional simulations. In addition to the three cases discussed in the main text, we consider the cases $\eta_0 = 0.35$ and $\eta_0 = 0.18$ m.

The subscript z_i next to a variable indicates that the variable is evaluated at $z = z_i$. The term in the left-hand side can be written as

$$\int_{z_i}^{z_\infty} \partial_t \langle \phi \rangle \, dz = \int_{z_i}^{z_\infty} \partial_t (\langle \phi \rangle - \phi_{bg}) \, dz = \frac{d}{dt} \int_{z_i}^{z_\infty} (\langle \phi \rangle - \phi_{bg}) \, dz + \frac{dz_i}{dt}(\langle \phi \rangle - \phi_{bg})_{z_i} \tag{A14}$$

where $\phi_{bg}(z)$ is the background profile describing the unperturbed atmosphere without the turbulent boundary layer. The last term in the right-hand side can be written as

$$\int_{z_i}^{z_\infty} \partial_z (\omega \langle \phi \rangle) \, dz = \int_{z_i}^{z_\infty} \partial_z [\omega(\langle \phi \rangle - \phi_{bg})] \, dz + \int_{z_i}^{z_\infty} d_z(\omega \phi_{bg}) \, dz \,, \tag{A15}$$

which yields

$$\int_{z_i}^{z_\infty} \partial_z (\omega \langle \phi \rangle) \, dz = -\omega_{z_i}(\langle \phi \rangle - \phi_{bg})_{z_i} + \int_{z_i}^{z_\infty} \rho_{ref} \, \omega d_z(\phi_{bg}/\rho_{ref}) \, dz \,, \tag{A16}$$

having used the continuity condition $\partial_z(\rho_{ref} \, \omega) = 0$. Substituting equations (A14) and (A16) into equation (A13), defining the lapse rate $\gamma_\phi \equiv -d_z(\phi_{bg}/\rho_{ref})$, and noting that $\omega = -\langle w \rangle$, we obtain equation (5) in section 3.2.

Appendix B: Sensitivity Studies

We have used two-dimensional simulations to estimate the sensitivity of the LWP with respect to changes in the Reynolds number and in the initial conditions. The dependence of the LWP on the Reynolds number is comparable to the dependence observed in the three-dimensional cases discussed in the main text. The LWP averaged between 3.4 and 4.1 hr increases from 19, to 36, and to 44 g/m² as the reference Kolmogorov scale decreases from 2.8, to 1.4, and to 0.7 m. Moreover, the actual values of LWP in the two-dimensional and three-dimensional cases are comparable with each other, which motivated us to consider two-dimensional cases with η_0 reduced by another factor of two and factor of 4. These cases correspond to Reynolds numbers $Re_0 = 31250$ and $Re_0 = 78125$, and to grid sizes $10,240 \times 2,560$ and $20,480 \times 5,120$, respectively. As observed in Figure B1, the LWP for $\eta_0 = 0.35$ m is initially larger than for $\eta_0 = 0.7$ m, but it becomes comparable after $t \approx 3$ hr. Reducing the Kolmogorov scale from $\eta_0 = 0.35$ to $\eta_0 = 0.18$ m, the LWP remains statistically the same. The LWP averaged between 3.4 and 4.1 hr is plotted in Figure B2 for all cases. Although results from two-dimensional simulations should be carefully extrapolated to three-dimensional simulations, the Reynolds number convergence observed in this figure further suggests that the Reynolds numbers that we can reach in simulations start to allow, to a certain extent, the extrapolation of results to atmospheric conditions.

The aim of the study of the sensitivity of the LWP with respect to the initial conditions was to assess the possibility of obtaining data between 3 and 4 hr at a higher Reynolds number using data from a lower Reynolds number as initial conditions to save computational time. We considered the fields at $t \approx 1.5$ hr in cases $\eta_0 = 2.8$ and $\eta_0 = 1.4$ m, interpolated the data into a grid with a grid spacing twice as small, and increased the Reynolds number by 2.5 to match the parameters that define the reference simulations $\eta_0 = 1.4$ and $\eta_0 = 0.7$ m, respectively. As seen in Figure B3, after ≈ 0.8 hr, which is about two large-eddy turnover times,
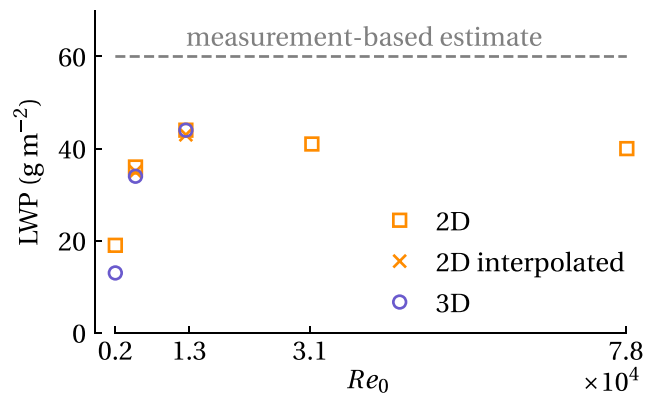
Figure B2. Convergence of liquid water path (LWP) averaged between 3.4 and 4.1 hr toward Reynolds number similarity.
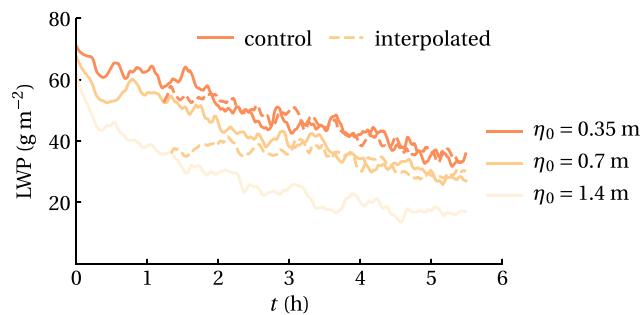

Figure B3. Sensitivity of liquid water path (LWP) to changes in initial conditions in two-dimensional simulations. In addition to the three cases discussed in the main text, we consider two cases $\eta_0 = 0.7$ and $\eta_0 = 1.4$ m initialized with interpolated data from simulations with a lower Reynolds number.

the LWP from simulations that are initialized with lower-Reynolds-number data becomes statistically the same as the LWP from simulations started earlier with random fields. The means between 3.4 and 4.1 hr are 35 and 43 g/m^2 for the former compared with 36 and 44 g/m^2 for the latter. This result justifies the use of lower-Reynolds-number data as initial conditions to save computational time for the analysis that we make in the main text.

References

Berner, A. H., Bretherton, C. S., & Wood, R. (2011). Large-eddy simulation of mesoscale dynamics and entrainment around a pocket of open cells observed in VOCALS RF06. *Atmospheric Chemistry and Physics*, *11*, 10,525–10,540.

Blossey, P. N., Bretherton, C. S., Zhang, M., Cheng, A., Endo, S., Heus, T., et al. (2013). Marine low cloud sensitivity to an idealized climate change: The CGILS LES intercomparison. *Journal of Advances in Modeling Earth Systems*, *5*, 234–258. https://doi.org/10.1002/jame.20025

Blossey, P. N., & Durran, D. R. (2008). Selective monotonicity preservation in scalar advection. *Journal of Computational Physics*, *227*, 5160–5183.

Bretherton, C. S., & Blossey, P. N. (2014). Low cloud reduction in a greenhouse-warmed climate: Results from Lagrangian les of a subtropical marine cloudiness transition. *Journal of Advances in Modeling Earth Systems*, *6*, 91–114. https://doi.org/10.1002/2013MS000250

Bretherton, C. S., Blossey, P. N., & Jones, C. R. (2013). Mechanisms of marine low cloud sensitivity to idealized climate perturbations: A single-LES exploration extending the CGILS cases. *Journal of Advances in Modeling Earth Systems*, *5*, 316–337. https://doi.org/10.1002/jame.20019

Bretherton, C. S., Macvean, M. K., Bechtold, P., Chlond, A., Cotton, W. R., Cuxart, J., et al. (1999). An intercomparison of radiatively driven entrainment and turbulence in a smoke cloud, as simulated by different numerical models. *Quarterly Journal of the Royal Meteorological Society*, *125*, 391–423.

Carpenter, M. H., Gottlieb, D., & Abarbanel, S. (1993). The stability of numerical boundary treatments for compact high-order finite-difference schemes. *Journal of Computational Physics*, *108*, 272–295.

Carpenter, M. H., & Kennedy, C. A. (1994). Fourth-order 2N-storage Runge-Kutta schemes (Tech. Rep. TM-109112). Hampton, VA: NASA Langley Research Center.

Chandrakar, K. K., Cantrell, W., Chang, K., Ciochetto, D., Ovchinnikov, D. N. M., Shaw, R. A., & Yang, F. (2016). Aerosol indirect effect from turbulence-induced broadening of cloud-droplet size distributions. *Proceedings of the National Academy of Sciences of the United States of America*, *113*, 14,243–14,248.

Chung, D., & Matheou, G. (2012). Direct numerical simulation of stationary homogeneous stratified sheared turbulence. *Journal of Fluid Mechanics*, *696*, 434–467.

de Lozar, A., & Mellado, J. P. (2014). Cloud droplets in a bulk formulation and its application for the buoyancy reversal instability. *Quarterly Journal of the Royal Meteorological Society*, *140*, 1493–1504.

de Lozar, A., & Mellado, J. P. (2015). Mixing driven by radiative and evaporative cooling at the stratocumulus top. *Journal of the Atmospheric Sciences*, *72*, 4681–4700.

de Lozar, A., & Muessle, L. (2016). Long-resident droplets at the stratocumulus top. *Atmospheric Chemistry and Physics*, *16*, 6563–6576.

de Roode, S. R., Sandu, I., van der Dussen, J. J., Ackerman, A. S., Blossey, P., Jarecka, D., et al. (2016). Large-eddy simulations of EUCLIPSE-GASS Lagrangian stratocumulus-to-cumulus transitions: Mean state, turbulence, and decoupling. *Journal of the Atmospheric Sciences*, *73*, 2485–2508.

Deardorff, J. W. (1970). Convective velocity and temperature scales for the unstable planetary boundary layer and for Rayleigh convection. *Journal of the Atmospheric Sciences*, *27*, 1211–1213.

Deardorff, J. W. (1980). Cloud top entrainment instability. *Journal of the Atmospheric Sciences*, *37*, 131–147.

Dimotakis, P. E. (2000). The mixing transition in turbulent flows. *Journal of Fluid Mechanics*, *409*, 69–98.

Domaradzki, J. A., Xiao, Z., & Smolarkiewicz, P. (2003). Effective eddy viscosities in implicit large eddy simulations of turbulent flows. *Physics of Fluids*, *15*, 3890–3893.

Dougherty, J. P. (1961). The anisotropy of turbulence at the meteor level. *Journal of Atmospheric and Solar-Terrestrial Physics*, *21*, 210–213.

Emanuel, K. A. (1994). *Atmospheric convection*. New York: Oxford University Press.

Faloona, I., Lenschow, D. H., Campos, T., Stevens, B., van Zanten, M., Bloomquist, B., et al. (2005). Observations of entrainment in eastern pacific marine stratocumulus using three conserved scalars. *Journal of the Atmospheric Sciences*, *62*, 3268–3284.

Flatau, P. J., Walko, R. L., & Cotton, W. R. (1992). Polynomial fits to saturation vapor pressure. *Journal of Applied Meteorology and Climatology*, *31*, 1507–1513.

Fox, D. G., & Lilly, D. K. (1972). Numerical simulation of turbulent flows. *Reviews of Geophysics and Space Physics*, *10*, 51–72.

Götzfried, P., Kumar, B., Shaw, R., & Schumacher, J. (2017). Droplet dynamics and fine-scale structure in a shearless turbulent mixing layer with phase changes. *Journal of Fluid Mechanics*, *814*, 452–483.

Grabowski, W. W., & Abade, G. (2017). Broadening of cloud droplet spectra through eddy hopping: Turbulent adiabatic parcel simulations. *Journal of the Atmospheric Sciences*, *74*, 1485–1493.

Grabowski, W. W., & Wang, L.-P. (2013). Growth of cloud droplets in a turbulent environment. *Annual Review of Fluid Mechanics*, *45*, 293–324.

Herbert, D. A., & de Bruyn Kops, S. M. (2006). Predicting turbulence in flows with strong stable stratification. *Physics of Fluids*, *18*, 066602.

Ivey, G. N., Winters, K. B., & Koseff, J. R. (2008). Density stratification, turbulence, but how much mixing? *Annual Review of Fluid Mechanics*, *40*, 169–184.

Jen-La Plante, I., Ma, Y.-F., Nurowska, K., Gerber, H., Khelif, D., Karpinska, K., et al. (2016). Physics of stratocumulus top (POST): Turbulence characteristics. *Atmospheric Chemistry and Physics*, *16*, 9711–9725.

Jones, C. R., Bretherton, C. S., & Blossey, P. N. (2014). Fast stratocumulus time scale in mixed layer model and large eddy simulation. *Journal of Advances in Modeling Earth Systems*, *6*, 206–222. https://doi.org/10.1002/2013MS000289

Katzwinkel, J., Siebert, H., & Shaw, R. (2012). Observation of self-limiting, shear-induced turbulent inversion layer above marine stratocumulus. *Boundary-Layer Meteorology*, *145*, 131–143.

Khairoutdinov, M., & Randall, D. A. (2003). Cloud resolving modeling of the ARM summer 1997 IOP: Model formulation, results, uncertainties, and sensitivities. *Journal of the Atmospheric Sciences*, *60*, 607–625.

Kumar, B., Schumacher, J., & Shaw, R. (2014). Lagrangian mixing dynamics at the cloudy-clear air interface. *Journal of the Atmospheric Sciences*, *71*, 2564–2580.

Kurowski, M. J., Malinowski, S. P., & Grabowski, W. (2009). A numerical investigation of entrainment and transport within a stratocumulus-topped boundary layer. *Quarterly Journal of the Royal Meteorological Society*, *135*, 77–92.

Lanotte, A. S., Seminara, A., & Toschi, F. (2009). Cloud droplet growth by condensation in homogeneous isotropic turbulence. *Journal of the Atmospheric Sciences*, *66*, 1685–1697.

Larson, V. E., Kotenberg, K. E., & Wood, N. B. (2007). An analytic longwave radiation formula for liquid layer clouds. *Monthly Weather Review*, *135*, 689–699.

Lele, S. K. (1992). Compact finite difference schemes with spectral-like resolution. *Journal of Computational Physics*, *103*, 16–42.

Lilly, D. K. (1967). The representation of small-scale turbulence in numerical simulation experiments, Proceedings of the IBM Scientific Computing Symposium on Environmental Sciences. IBM Form 320-1951.

Lilly, D. K. (1968). Models of cloud-topped mixed layers under strong inversion. *Quarterly Journal of the Royal Meteorological Society*, *94*, 292–309.

Lock, A. P. (2009). Factors influencing cloud area at the capping inversion for shallow cumulus clouds. *Quarterly Journal of the Royal Meteorological Society*, *135*, 941–952.

Margolin, L. G., & Rider, W. J. (2002). A rationale for implicit turbulence modeling. *International Journal for Numerical Methods in Fluids*, *39*, 821–841.

Matheou, G., & Chung, D. (2014). Large-eddy simulation of stratified turbulence. Part I: A vortex-based subgrid-scale model. *Journal of the Atmospheric Sciences*, *71*, 1863–1879.

McGibbon, J., & Bretherton, C. S. (2017). Skill of ship-following large-eddy simulations in reproducing magic observations across the northeastern Pacific stratocumulus to cumulus transition region. *Journal of Advances in Modeling Earth Systems*, *9*, 810–831. https://doi.org/10.1002/2017MS000924

Mellado, J. P. (2010). The evaporatively driven cloud-top mixing layer. *Journal of Fluid Mechanics*, *660*, 1–32.

Mellado, J. P. (2012). Direct numerical simulation of free convection over a heated plate. *Journal of Fluid Mechanics*, *712*, 418–450.

Mellado, J. P. (2017). Cloud-top entrainment in stratocumulus clouds. *Annual Review of Fluid Mechanics*, *41*, 145–169.

Mellado, J. P., & Ansorge, C. (2012). Factorization of the Fourier transform of the pressure-Poisson equation using finite differences in colocated grids. *ZAMM Journal of Applied Mathematics and Mechanics*, *92*, 380–392.

Mellado, J. P., Stevens, B., & Schmidt, H. (2014). Wind shear and buoyancy reversal at the top of stratocumulus. *Journal of the Atmospheric Sciences*, *71*, 1040–1057.

Mellado, J. P., Stevens, B., Schmidt, H., & Peters, N. (2010). Two-fluid formulation of the cloud-top mixing layer for direct numerical simulation. *Theoretical and Computational Fluid Dynamics*, *24*, 511–536.

Moeng, C.-H. (1986). Large-eddy simulation of a stratus-topped boundary layer. Part I: Structure and budgets. *Journal of the Atmospheric Sciences*, *43*, 2886–2900.

Moeng, C.-H. (2000). Entrainment rate, cloud fraction, and liquid water path of PBL stratocumulus clouds. *Journal of the Atmospheric Sciences*, *57*, 3627–3643.

Moin, P., & Mahesh, K. (1998). Direct numerical simulation: A tool in turbulence research. *Annual Review of Fluid Mechanics*, *30*, 539–578.

Monin, A. S., & Yaglom, A. M. (2007). *Statistical fluid mechanics. Mechanics of turbulence* (Vol. 1, p. 769). Mineola, New York: Dover Publications.

Naumann, A. K., & Seifert, A. (2016). Recirculation and growth of raindrops in simulated shallow cumulus. *Journal of Advances in Modeling Earth Systems*, *8*, 520–537. https://doi.org/10.1002/2016MS000631

Onishi, R., & Seifert, A. (2016). Reynolds-number dependence of turbulence enhancement on collision growth. *Atmospheric Chemistry and Physics*, *16*, 12,441–12,455.

Orszag, S. A., & Patterson, G. S. (1972). Numerical simulation of three-dimensional homogeneous isotropic turbulence. *Physical Review Letters*, *28*(2), 76–79.

Ozmidov, R. V. (1965). On the turbulent exchange in a stably stratified ocean. *Izv., Atmospheric and Oceanic Physics Series*, *1*, 853–860.

Pedersen, J. G., Malinowski, S. P., & Grabowski, W. W. (2016). Resolution and domain-size sensitivity in implicit large-eddy simulation of the stratocumulus-topped boundary layers. *Journal of Advances in Modeling Earth Systems*, *8*, 885–903. https://doi.org/10.1002/2015MS000572

Perrin, V., & Jonker, H. J. J. (2015). Lagrangian droplet dynamics in the subsiding shell of a cloud using direct numerical simulations. *Journal of the Atmospheric Sciences*, *72*, 4015–4028.

Pope, S. B. (2000). *Turbulent Flows*. Cambridge, UK: Cambridge University Press.

Pope, S. B. (2004). Ten questions concerning the large-eddy simulation of turbulent flows. *New Journal of Physics*, *6*(35), 1–24.

Pressel, K. G., Mishra, S., Schneider, T., Kaul, C. M., & Tan, Z. (2017). Numerics and subgrid-scale modeling in large eddy simulations of stratocumulus clouds. *Journal of Advances in Modeling Earth Systems*, *9*, 1342–1365. https://doi.org/10.1002/2016MS000778

Richter, D. H., & Veron, F. (2016). Ocean spray: An outsized influence on weather and climate. *Physics Today*, *69*, 34–39.

Rogallo, R. S., & Moin, P. (1984). Numerical simulation of turbulent flows. *Annual Review of Fluid Mechanics*, *16*, 99–137.

Rogers, R. R., & Yau, M. K. (1989). *A Short Course in Cloud Physics* (3rd ed.). Butterworth: Heinemann.

Sandu, I., & Stevens, B. (2011). On the factor modulating the stratocumulus to cumulus transition. *Journal of the Atmospheric Sciences*, *68*, 1865–1881.

Shaw, R. A. (2003). Particle-turbulence interactions in atmospheric clouds. *Annual Review of Fluid Mechanics*, *35*, 183–227.

Shima, S., Kusano, K., Kawano, A., Sugiyama, T., & Kawahara, S. (2009). The super-droplet method for the numerical simulation of clouds and precipitation: A particle-based and probabilistic microphysics model coupled with a non-hydrostatic model. *Quarterly Journal of the Royal Meteorological Society*, *135*, 1307–1320.

Smagorinsky, J. (1963). General Circulation Experiments with the primitive equations. *Monthly Weather Review*, *91*(3), 99–165.

Smolarkiewicz, P. K., & Margolin, L. G. (1998). MPDATA: A finite-difference solver for geophysical flows. *Journal of Computational Physics*, *140*, 459–480.

Stevens, B. (2002). Entrainment in stratocumulus-topped mixed layers. *Quarterly Journal of the Royal Meteorological Society*, *128*, 2663–2690.

Stevens, B., Feingold, G., Cotton, W. R., & Walko, R. L. (1996). Elements of the microphysical structure of numerically simulated nonprecipitating stratocumulus. *Journal of the Atmospheric Sciences*, *53*, 980–1006.

Stevens, B., & Lenschow, D. H. (2001). Observations, experiments and large-eddy simulations. *Bulletin of the American Meteorological Society*, *82*, 283–294.

Stevens, B., Lenschow, D. H., Faloona, I., Moeng, C.-H., Lilly, D. K., Blomquist, B., et al. (2003). On entrainment rates in nocturnal marine stratocumulus. *Quarterly Journal of the Royal Meteorological Society*, *129*(595), 3469–3493.

Stevens, B., Lenschow, D. H., Vali, G., Gerber, H., Bandy, A., Blomquist, B., et al. (2003). Dynamics and chemistry of marine stratocumulus—DYCOMS-II. *Bulletin of the American Meteorological Society*, *84*, 579–593.

Stevens, B., Moeng, C.-H., Ackerman, A. S., Bretherton, C. S., Chlond, A., de Roode, S., et al. (2005). Evaluation of large-eddy simulations via observations of nocturnal marine stratocumulus. *Monthly Weather Review*, *133*, 1443–1462.

Stevens, B., Moeng, C.-H., & Sullivan, P. P. (1999). Large-eddy simulation of radiatively driven convection: Sensitivities to the representation of the small scales. *Journal of the Atmospheric Sciences*, *56*, 3963–3984.

Stevens, B., Moeng, C.-H., & Sullivan, P. P. (2000). Entrainment and subgrid lengthscales in large-eddy simulations of atmospheric boundary layer flows. In R. Kerr & Y. Kimura (Eds.), *Developments in geophysical turbulence: Selected contributions to the IUTAM meeting*. Amsterdam: Kluwer.

Sullivan, P. P., & McWilliams, J. C. (2010). Dynamics of winds and currents coupled to surface waves. *Annual Review of Fluid Mechanics*, *42*, 19–42.

Sullivan, P. P., & Patton, E. G. (2011). The effect of mesh resolution on convective boundary layer statistics and structures generated by large-eddy simulations. *Journal of the Atmospheric Sciences*, *68*, 2395–2415.

Tennekes, H., & Lumley, J. L. (1972). *A first course in turbulence* (p. 300). Cambridge: MIT Press.

Turner, J. S. (1973). *Buoyancy effects in fluids*. Cambridge, UK: Cambridge University Press.

Uchida, J., Bretherton, C. S., & Blossey, P. N. (2010). The sensitivity of stratocumulus-capped mixed layers to cloud droplet concentration: Do LES and mixed-layer models agree? *Atmospheric Chemistry and Physics*, *10*, 4097–4109.

van Driel, R., & Jonker, H. J. J. (2010). Convective boundary layers driven by nonstationary surface heat fluxes. *Journal of the Atmospheric Sciences*, *68*, 727–738.

van der Dussen, J. J., de Roode, S. R., Ackerman, A. S., Blossey, P. N., Bretherton, C. S., Kurowski, M. J., et al. (2013). The GASS/EUCLIPSE model intercomparison of the stratocumulus transition as observed during ASTEX: LES results. *Journal of Advances in Modeling Earth Systems*, *5*, 483–499. https://doi.org/10.1002/10.1002/jame.20033

van der Dussen, J. J., de Roode, S. R., & Siebesma, A. P. (2014). Factors controlling rapid stratocumulus cloud thinning. *Journal of the Atmospheric Sciences*, *71*, 655–664.

Wood, R. (2012). Stratocumulus clouds. *Monthly Weather Review*, *140*, 2373–2423.

Yamaguchi, T., & Feingold, G. (2013). On the size distribution of cloud holes in stratocumulus and their relationship to cloud-top entrainment. *Geophysical Research Letters*, *40*, 2450–2454. https://doi.org/10.1002/grl.50442

Yamaguchi, T., Feingold, G., & Kazil, J. (2017). Stratocumulus to cumulus transition by drizzle. *Journal of Advances in Modeling Earth Systems*, *9*, 2333–2349. https://doi.org/10.1002/2017MS001104

Yamaguchi, T., & Randall, D. A. (2008). Large-eddy simulation of evaporatively driven entrainment in cloud-topped mixed layers. *Journal of the Atmospheric Sciences*, *65*, 1481–1504.

Yamaguchi, T., & Randall, D. A. (2012). Cooling of entrained parcels in a large-eddy simulation. *Journal of the Atmospheric Sciences*, *69*, 1118–1136.